Amyloid polymorphisms constitute distinct clouds of conformational variants in different etiological subtypes of Alzheimer's disease

Jay Rasmussen[a,b,c,1], Jasmin Mahler[a,c,1], Natalie Beschorner[a,c,1], Stephan A. Kaeser[a,b], Lisa M. Häsler[a,b], Frank Baumann[a,b], Sofie Nyström[d], Erik Portelius[e,f], Kaj Blennow[e,f], Tammaryn Lashley[g], Nick C. Fox[h], Diego Sepulveda-Falla[i,j,k], Markus Glatzel[i], Adrian L. Oblak[l], Bernardino Ghetti[l], K. Peter R. Nilsson[d], Per Hammarström[d], Matthias Staufenbiel[a], Lary C. Walker[m,n], and Mathias Jucker[a,b,2]

[a]Department of Cellular Neurology, Hertie Institute for Clinical Brain Research, University of Tübingen, 72076 Tübingen, Germany; [b]German Center for Neurodegenerative Diseases, 72076 Tübingen, Germany; [c]Graduate School of Cellular and Molecular Neuroscience, University of Tübingen, 72074 Tübingen, Germany; [d]Department of Physics, Chemistry and Biology, Division of Chemistry, Linköping University, SE-581 83 Linköping, Sweden; [e]Institute of Neuroscience and Physiology, Department of Psychiatry and Neurochemistry, University of Gothenburg, SE-431 80 Mölndal, Sweden; [f]Clinical Neurochemistry Laboratory, Sahlgrenska University Hospital, SE-431 80 Mölndal, Sweden; [g]Queen Square Brain Bank for Neurological Diseases, Department of Molecular Neuroscience, Institute of Neurology, University College London, London WC1N 1PJ, United Kingdom; [h]Dementia Research Centre, University College London, London WC1N 3BG, United Kingdom; [i]Institute of Neuropathology, University Medical Center Hamburg-Eppendorf, 20246 Hamburg, Germany; [j]Neuroscience Group of Antioquia, University of Antioquia, 1226 Medellín, Colombia; [k]Faculty of Medicine, University of Antioquia, 1226 Medellín, Colombia; [l]Department of Pathology and Laboratory Medicine, Indiana University School of Medicine, Indianapolis, IN 46202; [m]Department of Neurology, Emory University, Atlanta, GA 30322; and [n]Yerkes National Primate Research Center, Emory University, Atlanta, GA 30329

Edited by Stephen M. Strittmatter, Yale University School of Medicine, New Haven, CT, and accepted by Editorial Board Member Solomon H. Snyder October 24, 2017 (received for review July 26, 2017)

The molecular architecture of amyloids formed in vivo can be interrogated using luminescent conjugated oligothiophenes (LCOs), a unique class of amyloid dyes. When bound to amyloid, LCOs yield fluorescence emission spectra that reflect the 3D structure of the protein aggregates. Given that synthetic amyloid-β peptide (Aβ) has been shown to adopt distinct structural conformations with different biological activities, we asked whether Aβ can assume structurally and functionally distinct conformations within the brain. To this end, we analyzed the LCO-stained cores of β-amyloid plaques in postmortem tissue sections from frontal, temporal, and occipital neocortices in 40 cases of familial Alzheimer's disease (AD) or sporadic (idiopathic) AD (sAD). The spectral attributes of LCO-bound plaques varied markedly in the brain, but the mean spectral properties of the amyloid cores were generally similar in all three cortical regions of individual patients. Remarkably, the LCO amyloid spectra differed significantly among some of the familial and sAD subtypes, and between typical patients with sAD and those with posterior cortical atrophy AD. Neither the amount of Aβ nor its protease resistance correlated with LCO spectral properties. LCO spectral amyloid phenotypes could be partially conveyed to Aβ plaques induced by experimental transmission in a mouse model. These findings indicate that polymorphic Aβ-amyloid deposits within the brain cluster as clouds of conformational variants in different AD cases. Heterogeneity in the molecular architecture of pathogenic Aβ among individuals and in etiologically distinct subtypes of AD justifies further studies to assess putative links between Aβ conformation and clinical phenotype.

Alzheimer | amyloid | neurodegeneration | prion | strains

Despite a common origin in the structural corruption and accumulation of specific proteins, the clinical and pathological phenotype of Alzheimer's disease (AD) exhibits conspicuous variability within and among patients (1–4). The amyloid cascade hypothesis posits that the seminal event in the pathogenesis of AD is the misfolding and aggregation of the amyloid-β peptide (Aβ) (5, 6). In vitro investigations have found that Aβ can aggregate into diverse amyloid structures that can impose their conformational characteristics onto naive synthetic forms of the protein (7, 8). In Aβ precursor protein (APP)-transgenic mouse models, polymorphisms of aggregated Aβ have been demonstrated that subsequently could be propagated to naive and susceptible host mice (9–11).

Recent work in humans suggests that Aβ can aggregate into structural variants with distinct pathobiological traits. One such study used extracted fibrils from AD brains to seed the aggregation of synthetic Aβ in vitro. The resulting synthetic descendants of aggregated Aβ from brain samples provided indirect evidence for structural heterogeneity of Aβ among AD brains; in addition, the findings suggested that Aβ assumes a single, dominant conformation within a given brain (12, 13). Another investigation has shown that the biophysical features of aggregated Aβ differ significantly in patients with rapidly progressive AD compared with those with normally progressive disease, indicative of distinct molecular structures of Aβ (14). In an exceptional example of Aβ aggregate structural variation in AD, a patient was described as having an extraordinarily high Aβ burden but a paucity of high-affinity Pittsburgh compound B (PiB) binding sites (15). More recently, X-ray microdiffraction analysis of

Significance

The clinical and pathological variability among patients with Alzheimer's disease (AD) remains largely unexplained. Evidence is growing that this heterogeneity may be influenced by the heterogeneous molecular architecture of misfolded amyloid-β peptide (Aβ) in the brain. To test this hypothesis, we used unique fluorescent ligands to interrogate the molecular structure of Aβ in amyloid plaques from patients who had died with etiologically distinct subtypes of AD. We found that Aβ-amyloid plaques in the brain cluster as clouds of conformational variants that differ among certain subtypes of AD. The conformational features of AD plaques were partially transmissible to transgenic mice in a seeding paradigm, suggesting a mechanism whereby different molecular strains of Aβ propagate their features within the brain.

Author contributions: K.B., N.C.F., M.G., B.G., K.P.R.N., P.H., M.S., L.C.W., and M.J. designed research; and J.R., J.M., N.B., S.A.K., L.M.H., F.B., S.N., E.P., T.L., D.S.-F, and A.L.O. performed research.

The authors declare no conflict of interest.

This article is a PNAS Direct Submission. S.M.S. is a guest editor invited by the Editorial Board.

[1]J.R., J.M., and N.B. contributed equally to this work.

[2]To whom correspondence should be addressed. Email: mathias.jucker@uni-tuebingen.de.

This article contains supporting information online at www.pnas.org/lookup/suppl/doi:10.1073/pnas.1713215114/-/DCSupplemental.

individual AD brain tissue samples indicated that the amyloid arrangement of Aβ is polymorphic within and among plaques (16).

Morphologically at the light-microscopic level, it is well documented that amyloid plaques in AD brains present with phenotypic variation that typically ranges from diffuse to dense-cored plaques (17–24). How such morphotypes are linked to the molecular conformation of the amyloid has not been established.

The characterization of amyloid has been facilitated by a new class of dyes known as luminescent conjugated oligothiophenes (LCOs; or luminescent conjugated polythiophenes) (25, 26). LCO dyes bind to the repetitive cross–β-sheet structures of amyloid fibrils and display spectral differences based on the twisting of the flexible LCO backbone (25, 27). Additionally, it was found that certain LCOs compete with a Congo red analog (X-34) for binding to recombinant Aβ-amyloid fibrils as well as AD brain-derived Aβ, but they do not compete for the PiB binding site (28). It has been demonstrated that LCOs can detect molecular differences in Aβ plaque structure in different APP-transgenic mouse models (10), and in Aβ aggregated in vitro at different stages of fibrillization (25, 29, 30).

We hypothesized that the phenotypic and histopathological variability of AD results, at least in part, from variation in the molecular architecture of aggregated Aβ. To this end, we used LCOs and biochemical analyses to evaluate the variation and structural properties of amyloid in the plaques of patients with AD from different etiological backgrounds [familial forms; sporadic forms, including the posterior cortical atrophy (PCA) variant of AD (PCA-AD); and a unique PiB-negative AD case]. Our results provide evidence for the existence of heterogeneous Aβ-amyloid structures that cluster as clouds across different patients with AD while encoding conformational characteristics that can be biologically propagated.

Results

Spectral Characteristics of Plaque Amyloid in AD Brains. We evaluated plaque amyloid in tissue sections from a cohort of patients with AD of various etiologies, including familial mutation carriers for *APP* (*V717I*) and *PSEN1* (*A431E*, *F105L*, and *E280A*), as well as cases of typical sporadic AD (sAD) and sporadic PCA-AD (Table S1). A double-stain combination with two LCOs, quadro-formyl thiophene acetic acid (qFTAA) and hepta-formyl thiophene acetic acid (hFTAA) (29, 30) (*Methods*), was used to label amyloid plaques in fresh-frozen brain sections. Subsequently, the dense (congophilic) cores of amyloid plaques were spectrally analyzed for fluorescence emission characteristics (Figs. S1 and S2). Three brain regions, the midtemporal gyrus (temporal), pericalcarine gyri (occipital), and midfrontal gyrus (frontal), were investigated for each patient (Fig. 1*A*). Preliminary visual inspection under the fluorescence microscope revealed obvious variation in plaque appearance even within a tissue section (Fig. 1*B*).

To determine how the molecular structure of plaque amyloid varies among brains and brain regions, the mean emission spectra were calculated for all plaques in each brain region of all subjects. Pairwise comparisons between individual patients were then performed using a Euclidean distance calculation (Fig. 1 *C* and *D*). This analysis revealed that the spectral signatures of plaque amyloid in familial *APP V717I* and *PSEN1 A431E* mutation carriers were most different from the other groups (Fig. 1*C*). Statistical analysis of the ratio of the emission peaks for qFTAA (502 nm) and hFTAA (588 nm) in individual plaque cores confirmed that the *APP V717I* and *PSEN1 A431E* groups were significantly different from most other groups (Fig. 1*E*). A difference was also found between sAD and PCA-AD cases (Fig. 1*E*). Of note, however, was the striking variability within the sAD group (Fig. 1 *C* and *E*), with one of the samples with a high LCO spectral ratio being a previously described case with reduced high-affinity binding of PiB (Fig. 1 *C* and *E*).

To further interrogate the variability in LCO spectra among the groups, all data points from the analysis based on the correlation of fluorescence intensity at 502 nm and 588 nm were examined (Fig. 1*F*). Again, the spectral signatures of plaque amyloid in the different patient groups segregated into noticeable clouds that partially overlapped each other (Fig. 1*F*).

Amyloid Plaque Spectral Characteristics Compared with Other Metrics. To determine whether the results from the LCO spectral analysis of plaques could be explained by factors that affect amyloid deposition in the brain, LCO ratios were related to apolipoprotein E (ApoE) genotype, subject age at death, and postmortem interval (PMI) (Fig. 2). Only sAD and PCA-AD samples were used to remove obvious confounding effects that the familial mutations might have on the comparison (e.g., younger mean age at death). No correlation was found between spectral ratio and ApoE status or subject age at death (Fig. 2 *A*–*C*). The correlation found between the spectral ratio and the PMI disappeared when sAD cases and PCA-AD cases were analyzed separately, reflecting the overall longer PMI for the PCA-AD samples (Fig. 2*C*). Thus, ApoE, age at death, and PMI are not crucial factors for the observed LCO spectral differences.

To assess whether the LCO results are related to the total Aβ load or the deposited Aβ species, Aβ was analyzed biochemically (Fig. S2). Overall, samples from the *PSEN1 A431E* group had higher Aβ levels than all other groups. The ratio of Aβ42/40 was higher in the *APP V717I* familial mutation carriers compared with the *PSEN1* mutation carriers (Fig. S2). Neither the amount of Aβ nor the Aβ42/40 ratio differed significantly across the three neocortical regions; furthermore, the LCO spectra were not significantly associated with either total Aβ or the Aβ42/40 ratio when the analysis was confined to sAD and PCA-AD samples (Fig. 2 *D* and *E*).

Proteinase K (PK) resistance has been linked to pathogenic conformations of Aβ in mouse models and AD brains (11, 31, 32). To determine whether the LCO spectral signatures of the plaque cores are associated with protease sensitivity, the resistance of aggregated Aβ to proteolysis over time was evaluated (Fig. S2). No differences among patient groups were observed (Fig. S2). Furthermore, when only sAD and PCA-AD cases were considered, there was no significant correlation between the plaque spectral ratio and Aβ PK resistance (Fig. 2*F*).

Amyloid Plaque Spectral Characteristics Are Transmissible to Experimental Mouse Models. We next asked whether the LCO spectral properties of amyloid plaques can be propagated in vivo by the prion-like process of molecular conformational templating. To this end, cortical extracts from AD groups showing the most distinct LCO spectra, namely, *APP V717I*, *PSEN1 A431E*, and sAD, in addition to the unique PiB-negative sAD case, were injected into the hippocampus of young APP23-transgenic mice (Fig. 3). APP23 mice were used for this analysis because they have recently been characterized in a seeding activity bioassay in which the precise biological activity of brain extracts was assessed (33). Before injection, all extracts were pooled for each AD group and the Aβ concentration was adjusted to 7.5 pg/μL. Since we found that the LCO spectral characteristics of plaques did not differ significantly among the three brain regions, we arbitrarily chose temporal cortical samples as the source of Aβ seeds.

Inoculated APP23 mice were analyzed 6 mo after injection (Fig. 3*A*). In all mice, Aβ deposition was induced in the hippocampus (primarily the dentate gyrus) as reported previously (9, 33). While this regional pattern of induction was not discernibly different among the groups, the amount of induction showed remarkable differences, with mice injected with *APP V717I* and typical sAD extracts manifesting at least twice as much induced Aβ deposition as mice injected with material from *PSEN1 A431E* donors or from the PiB-refractory sAD donor (Fig. 3 *A* and *B*).

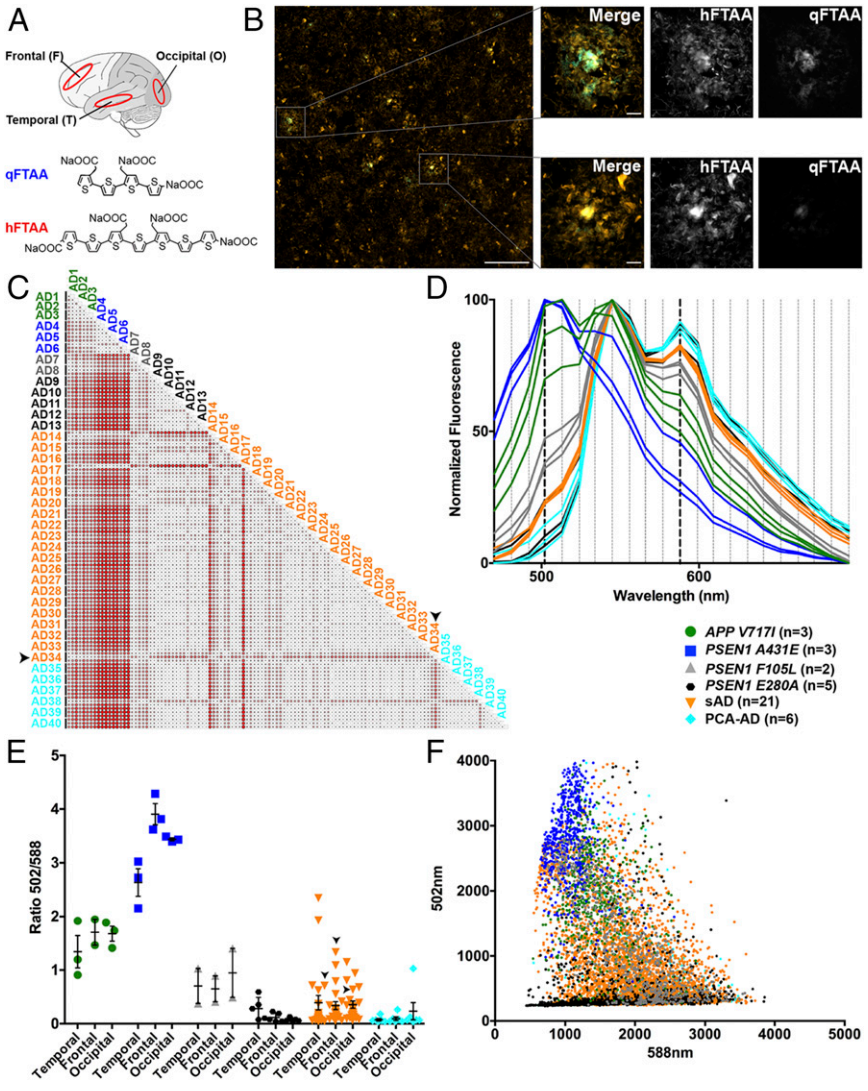

Fig. 1. Subtypes of AD display distinguishable clouds of amyloid conformational variants. (*A*) Combination of two LCOs, qFTAA and hFTAA, was used to stain Aβ plaques in three different neocortical regions (temporal: midtemporal gyrus, T; occipital: pericalcarine gyri, O; frontal: midfrontal gyrus, F) of postmortem brain tissue from familial AD (*APP V717I*, *PSEN1 A431E*, *PSEN1 F105L*, and *PSEN1 E280A*), typical sAD, and sporadic PCA-AD cases. (*B*) Shown is an LCO-stained section of the temporal cortex from a patient with sAD (AD16; also patient information in Table S1). Note that a variety of different fluorescence emission patterns are present in a single brain sample. (Scale bars: *Left*, 200 μm; *Right*, 20 μm.) (*C* and *D*) Plaques were randomly selected, and for each plaque core, the fluorescence intensity was measured at 22 wavelengths to produce a continuous fluorescence spectrum (40–60 plaques were analyzed per region for each brain sample; also Fig. S1). Each line in *D* represents the mean spectrum for a particular brain area in all patients in a given subgroup. A heat map depicting the difference of Euclidean distances between the mean spectra (of all 22 fluorescence measurements) for brain regions of individual patients is shown in *C*. Larger and more darkly colored circles represent more dissimilar spectra. The labels represent patient numbers with the temporal, occipital, and frontal regions repeating as sets of three (from top to bottom). Note the variability within the sAD group, with some regions yielding emission spectra more similar to those of the familial groups (for AD2, only temporal and occipital cortex tissue was available for analysis). (*E*) For statistical analysis, the fluorescence intensity at 502 nm and 588 nm (which represent the fluorescence emission peaks of qFTAA and hFTAA, respectively; Fig. S1*C*) was analyzed for each region of each patient. Two-way ANOVA (brain region × AD subtype) revealed a significant effect for subtype [$F_{(5,101)} = 33.07$, $P < 0.0001$], but not for brain region [$F_{(2,101)} = 0.0681$, $P = 0.9343$] or interaction between region and subtype [$F_{(10,101)} = 0.7829$, $P = 0.6451$]. Tukey's multiple comparisons revealed significant differences between *APP V717I* vs. *PSEN1 E280A*, sAD and PCA-AD; *PSEN1 A431E* vs. *PSEN1 F105L*, *PSEN1 E280A*, sAD and PCA-AD; *PSEN1 F105L* vs. *PSEN1 E280A*, sAD and PCA-AD; and sAD vs. PCA-AD (all probabilities at least $P < 0.05$). An exceptional sAD case, AD34 (denoted by arrows in *C* and *E*), is a previously described case with reduced high-affinity binding of the PiB radioligand (15). Error bars represent the SEM. (*F*) Scatter plot of all plaques analyzed using fluorescence at 588 nm vs. 502 nm per AD subgroup reveals that plaque spectral properties within the AD subgroups occupy distinct clouds, which overlap between AD subgroups.

Strikingly, when brain sections from the recipient mice were stained using the same LCO protocol as that used for the human tissue (Fig. 1), quite remarkable differences in the emission spectra of individual plaque cores were observed (Fig. 3*A*). The mean emission spectra of all seeded hippocampal plaque cores were computed for each injected mouse, and a Euclidean distance calculation was applied to determine differences (Fig. 3*C*). Similar to the LCO spectral patterns in plaques from the human donors, seeded amyloid in the *PSEN1 A431E*-injected mice was most different from that in the sAD groups, albeit with more variation (Fig. 3 *C* and *D*). For statistical comparison of the experimental groups, the 502-nm/588-nm spectral ratio was calculated for each plaque core, and the mean ratios for each injected mouse were computed (Fig. 3 *D* and *E*). The spectral ratios in the different groups of seeded host mice displayed relatively similar patterns to those in the donor humans (compare Figs. 1*E* and 3*E*); the group difference was statistically significant between *PSEN1 A431E*- and sAD-seeded mice, but the other group differences did not reach statistical significance. The amount of induced Aβ deposition did not correlate with the spectral ratio, suggesting these two factors are independent (Fig. 3*F*). As with the human tissue, all plaque cores analyzed in the mice were plotted based on the fluorescence intensity at 502 nm against 588 nm (Fig. 3*G*). The plaques in seeded mice occupied similar clouds within an injection group, although these clouds showed more overlap in the injected mice than in the original human tissue (Fig. 1), suggestive of differential host–agent interactions (9).

Discussion

The extraordinary phenotypic variability of AD (1–3) currently defies explanation. It is likely that many factors are involved, including the age at disease onset, location of the initial abnormalities in the brain and their pattern of spread, the inflammatory response to the lesions, and the presence of comorbid conditions. The present findings support growing evidence that the heterogeneity of AD may also be influenced by the heterogeneous molecular architecture of misfolded Aβ in the brain.

Using synthetic Aβ that was aggregated in vitro, multimeric Aβ assemblies have been shown to assume diverse tertiary and quaternary structures (13, 34–37). These findings have greatly augmented our understanding of Aβ fibril structure, but their relevance to the pathobiology of Aβ in vivo, in the native disease

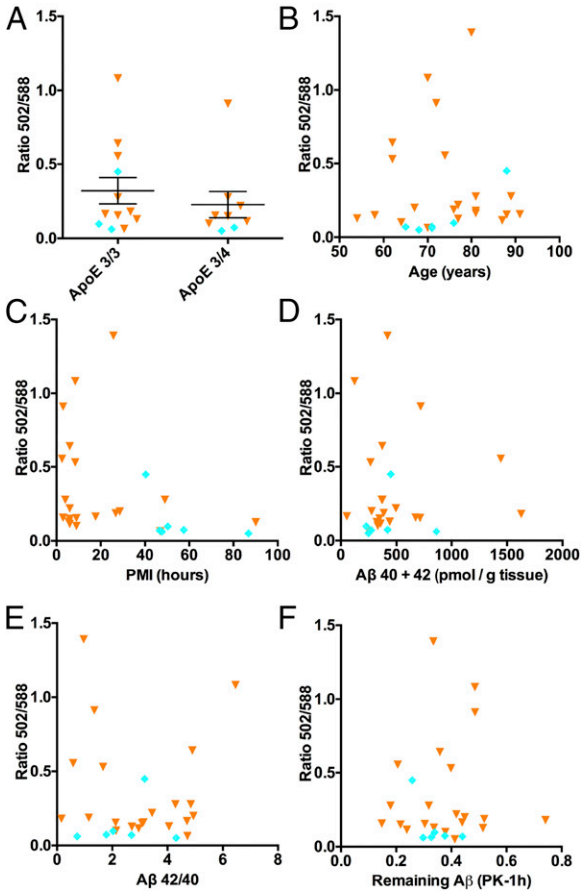

Fig. 2. Spectral properties of LCO-labeled amyloid plaques are not explained by ApoE genotype, patient age, PMI, or Aβ biochemistry. (*A*) LCO spectral ratio of fluorescence at 502 nm and 588 nm separated into ApoE genotype subgroups (mean of the three regions; Fig. 1*E*; only subjects with sAD and PCA-AD were used to remove the confounding effects of the familial mutations on the data; orange triangles, sAD; cyan diamonds, PCA-AD). The Mann–Whitney test was used to determine significance between ApoE 3/3 vs. 3/4 cases ($P = 0.4221$). Error bars represent the SEM. (*B*) LCO spectral ratio vs. patient age. Nonparametric Spearman correlation: $P = 0.38$. (*C*) LCO spectral ratio vs. PMI. Nonparametric Spearman correlation: $P = 0.29$ for PCA-AD and $P = 0.32$ for sAD. (*D* and *E*) LCO spectral ratios vs. ELISA measurements (mean of all brain regions) of Aβ 40 + 42 and the Aβ42/40 ratio (Aβ measurements are shown in Fig. S2). Nonparametric Spearman correlation analysis yielded $P = 0.26$ and $P = 0.81$, respectively. (*F*) LCO spectral ratio vs. Aβ remaining after 1 h of digestion with PK (mean of all brain regions). Nonparametric Spearman correlation: $P = 0.78$. Detailed results for PK digestion are shown in Fig. S3.

state, remains uncertain (38). For instance, in most cases, these experiments involved the analysis of a single isoform of Aβ, either 40 aa or 42 aa long, whereas there are multiple isoforms, fragments, and posttranslational modifications of Aβ in the living brain (39, 40).

Tycko and coworkers (12, 13) have demonstrated that Aβ derived from different cases of AD is able to induce synthetic Aβ to assemble into corresponding structural "strains," and the authors suggest that a single Aβ structure predominates in a particular AD brain. Our observations generally support the concept of a predominant, case-specific Aβ strain in that the mean LCO spectral emission of plaque cores (where the Aβ adopts an amyloid conformation) was similar in different cortical regions of each patient, regardless of the AD subtype. However, direct microscopic analysis of individual plaque cores with LCOs allowed us to determine that minor populations of Aβ aggregates with different molecular architectures also are present within a given AD brain. We therefore speculate that the presence of these structural variants in other investigations (12, 13) may have been masked by the conformational selection and in vitro propagation of a dominant strain in preparation for the NMR analysis. In support of this possibility, and in agreement with our findings, X-ray microdiffraction analysis has revealed structural polymorphism among amyloid plaques within the same tissue section (16).

In light of the intra- and interindividual variability in the LCO spectral characteristics of plaque amyloid, it is remarkable that we still found differences among patient subgroups, particularly between some of the familial AD and sAD cases (note that the familial AD mutations in the present study do not change the Aβ sequence). Neuropathological analyses also have revealed differences in plaque morphotypes between some familial AD mutations and sAD (18, 20, 23). However, while these observations were made on Aβ-immunostained plaques, our LCO-based spectral analysis was confined to the core of the plaque, and thus to Aβ in the amyloid conformation.

We were somewhat surprised to observe differences in the amyloid spectral characteristics between typical patients with sAD and patients with the PCA variant of AD. Both the regional distribution of amyloid and the clinical phenotype are different in PCA-AD and sAD (41). A previous NMR analysis did not indicate molecular structural differences between PCA-AD and sAD (13), but, as noted above, the analysis could have been confounded by conformational selection of Aβ species best suited for the seeded in vitro growth of fibrils. The clinicopathological distinctiveness of PCA-AD appears to result, in part, from a disease-specific site of origin and/or pattern of Aβ dissemination (41), but our findings indicate that the molecular architecture of misfolded Aβ may also play a role. Similarly, in a rapidly progressive subtype of AD, there is biochemical evidence for increased conformational heterogeneity of Aβ42 (14), and a recent NMR study using seeded growth of synthetic Aβ fibrils from brain-derived material supports this finding (13).

In the present study, the LCO spectral characteristics of amyloid in plaques did not correspond in a consistent way to the PK resistance or the abundance of the two major Aβ species (Aβ40 and Aβ42) in tissue homogenates. One possible explanation for this is that the spectral analysis and biochemical tests do not probe identical populations of Aβ [i.e., the amyloid core (LCOs) vs. the total pool of aggregated Aβ (biochemistry)]. Another possibility is that variation in amyloid structure revealed by the LCO spectral analysis is more sensitive at identifying subtle differences that biochemical analyses currently are unable to detect. Elucidation of the mechanisms underlying the architectural variability of Aβ in plaques could reveal pathogenically important targets for the development of personalized treatments for AD.

LCO binding and spectra are dependent on the orientation, side-chain interactions, and packing of amyloid fibrils, and the ability of LCOs to recognize amyloid features in protein pathologies has been well characterized (25). These ligands thus are exquisitely sensitive indicators of molecular architectural differences in proteopathic fibrils, for example, the strain-like diversity of prion protein aggregates (42). In recent studies, it has been shown that the arrangement and packing of Aβ-amyloid fibrils influence the spectral output of the LCOs, especially when the ligands are used in combination (29, 30, 43). Since LCO spectra indicate the presence of different structural conformations of Aβ, we predicted from previous experiments that these properties should be transmissible to susceptible hosts (44). Our studies in APP-transgenic mice confirm that Aβ-rich brain extracts from different subtypes of AD seed Aβ deposits that are correspondingly differentiable using LCOs. The LCO spectral traits of amyloid in the seeded transgenic mice did not perfectly mirror those of the human donor tissue; however, this is expected because both

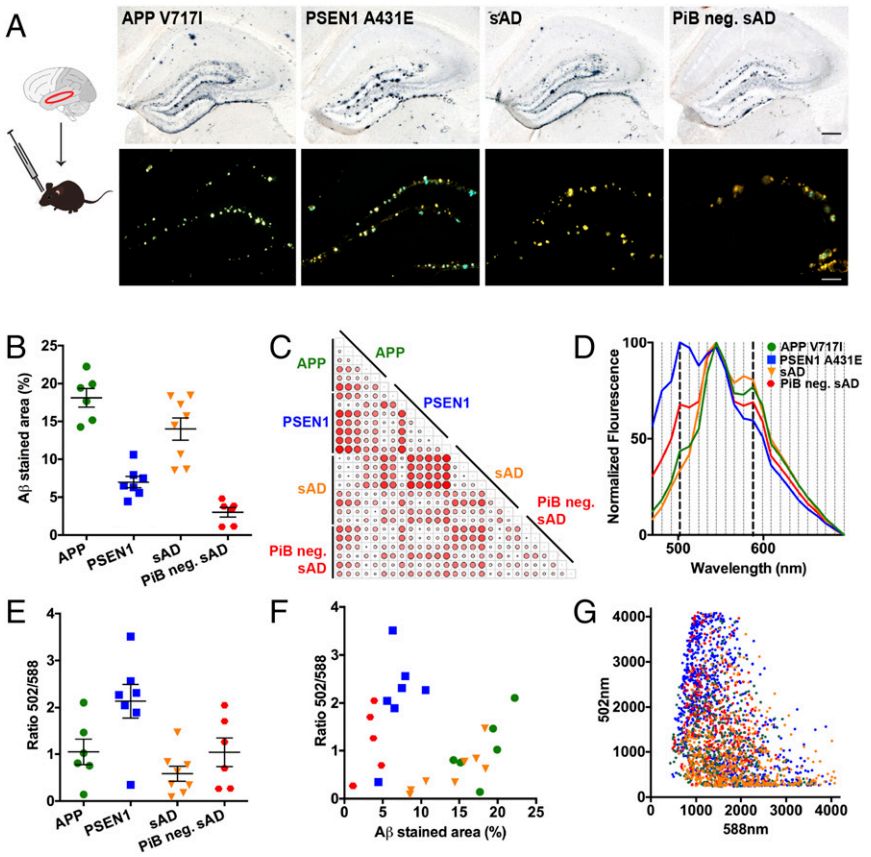

Fig. 3. Variant conformations of aggregated Aβ can be induced by exogenous seeding in APP-transgenic mice. (*A*) Seeding extracts were prepared from the middle temporal gyrus of pooled ($n = 3$) brain samples from human *APP V717I*, *PSEN1 A431E*, sAD [AD15, AD16, and AD24; patients collected in the same year at the same site (Emory University)] and a single PiB-refractory sAD case (AD34) (Fig. 1 and Table S1). Aβ concentrations of the seeding extracts were adjusted to 7.5 pg/μL (*Methods*). Extracts were injected into young (4-mo-old) female APP23 mice [*APP V717I* ($n = 6$), *PSEN1 A431E* ($n = 7$), sAD ($n = 8$), and PiB-negative (neg.) sAD ($n = 6$)]. Brains of recipient mice were analyzed 6 mo after injection. Induced Aβ deposition in the hippocampus was stained with a polyclonal Aβ antibody (*Top*) or the LCO double-staining protocol (*Bottom*). (Scale bars: *Top*, 200 μm; *Bottom*, 50 μm.) (*B*) Stereological quantification of Aβ-immunostained area in the hippocampus. The Kruskal–Wallis test followed by Dunn's multiple comparison test revealed significant differences in the degree of induction between *APP V717I* vs. *PSEN1 A431E* ($P < 0.05$) donors, PiB-neg. sAD vs. *APP V717I* donors ($P < 0.001$), and PiB-neg. sAD vs. sAD donors ($P < 0.01$). Error bars represent SEM. (*C*) Heat map of the Euclidean distance between LCO spectra calculated for each mouse (details are provided in Fig. 1). Larger and more darkly colored circles represent more dissimilar spectra. (*D*) Mean LCO fluorescence spectra of induced plaque cores for mice injected with different human extracts (20–30 plaques were analyzed per mouse; details are provided in Fig. 1). (*E*) For statistical analysis, the mean ratio of the fluorescence intensity at 502 nm and 588 nm was calculated for each mouse. The Kruskal–Wallis test followed by Dunn's multiple comparison test revealed significantly different spectral signatures in plaques seeded by *PSEN1 A431E* vs. sAD brain extracts ($P < 0.05$). Error bars represent the SEM. (*F*) Amount of Aβ induction did not correlate with the LCO spectral ratio of the induced amyloid (nonparametric Spearman correlation, $P = 0.9687$). (*G*) Scatter plot of LCO fluorescence spectra emitted by all plaques analyzed in seeded mice demonstrates an overall preservation of clustering among the groups, although the group differences were less distinct compared with plaque spectra in the original human donor samples (Fig. 1).

the agent and host influence the propagation of Aβ and the characteristics of the resulting deposits (9). In addition, the mice were seeded with extracts of brain tissue, which may have a seed composition that differs from that in the plaque cores. The existence of LCO spectral clouds that only partially recapitulate those of the AD donors thus may reflect the composition of seeds in the donor extract as well as the Darwinian selection of different Aβ strains in the host mice (45).

The spectral properties of LCOs bound to plaques change as APP-transgenic mice grow older, suggestive of age-related conformational rearrangement of the Aβ (30). Thus, it is possible that the spectral variation of plaques in individual patients with AD at least partially reflects the presence of plaques of different ages. The AD brains analyzed in the present study were all from patients with end-stage disease, at which point amyloid, per se, may no longer be the primary driver of the disease (46). Nevertheless, the deposited amyloid shows remarkable LCO spectral variability among patients with sporadic end-stage AD. Furthermore, the LCO spectral signals detected within an individual brain, although generally similar in the three cortical regions, constitute a cloud of variable emission spectra. It is possible that the composition of the amyloid may be more complex late in the pathogenic process than at earlier time points. If so, the LCO spectra might reveal more clearly differentiable disease patterns in the earlier stages. Analysis of incipient amyloid plaques in persons who died of other causes before the onset of AD symptoms will be informative in this regard. Finally, it will be important to establish the relationship between the variant molecular structure of plaque cores and the pathobiologically potent oligomeric forms of Aβ (31, 47).

The present findings have several implications for diagnostics and treatment. Variations in amyloid structure are likely a complicating factor when determining the distribution and severity of Aβ deposition by PET imaging in patients with AD, as demonstrated by an unusual case of AD with very high Aβ levels in the brain but negligible high-affinity binding of PiB (15). We found that the plaque cores in this case displayed an LCO spectral pattern that differed from that of most other sAD cases. If antibody binding to Aβ is similarly influenced by the molecular architecture of the misfolded protein, it is conceivable that a particular monoclonal antibody might fail to recognize the full range of Aβ aggregates that can arise within a brain and among different patients. Thus, it may be advantageous to use multiple antibodies to create a "polyclonal" mixture for treatment of Aβ pathology. Finally, future work should investigate the therapeutic potential of LCOs for AD and other proteopathies, as has been shown for prion disease (27), and, additionally, determine the feasibility of using LCOs to examine Aβ aggregates in bodily fluids such as cerebrospinal fluid and blood to augment the personalized diagnosis of AD.

Methods

Patient Samples. Fresh tissue samples were obtained from the midtemporal gyrus (temporal), pericalcarine gyri (occipital), and midfrontal gyrus (frontal) of 40 clinically and pathologically diagnosed AD cases (Table S1). The tissues were acquired under the proper Institutional Review Board protocols from the Tübingen Review Board for the work in the Queen Square Brain Bank at University College London samples (202/2016BO2), the Emory University Alzheimer's Disease Research Center to do the work on these samples (IRB 00045782), and the University of Antioquia, Medellin, Colombia (09-10-232). Informed consent was given by families (see *SI Methods* for details).

LCO Staining Spectral Analysis. Two LCO variants, qFTAA and hFTAA, were used to stain fresh-frozen tissue (30). Amyloid plaques were randomly chosen, and continuous emission spectra were acquired (Figs. S1 and S2). Only the dense cores of plaques were analyzed. Details are provided in *SI Methods*.

Aβ Quantification, Mass Spectrometry, and PK Digestion. For Aβ quantification, human tissue was extracted with 70% formic acid. Extracts were also analyzed by targeted mass spectrometry for Aβ (48). PK digestion was carried out on fresh tissue at 37 °C for 0, 1, 2, and 4 h and analyzed with Aβ immunoblots. Details are provided in *SI Methods*.

In Vivo Inoculations of the Mice. Seeding extracts were generated from the middle temporal gyrus (33). Pooled extracts [*APP V717I* (AD1–3), *PSEN1 A431E* (AD4–6), and typical sAD (AD15, AD16, and AD24)] and the distinct PiB-negative sAD case (AD34) (Table S1) were adjusted to the same Aβ concentration. Intrahippocampal injections were done in 4-mo-old APP23 mice (49). After 6 mo of incubation, brain sections were Aβ-immunostained and quantified (50, 51). Sections were also stained with the LCOs. All mouse experiments were approved by the local animal care and use committee in Baden-Württemburg, Germany (Regierungspräsidium Tübingen). Details are provided in *SI Methods*.

Statistical Analysis. GraphPad Prism (v.5) was used for statistical analyses. R (v. 3.3.2) was used for Euclidean distances. Details are provided in *SI Methods*.

ACKNOWLEDGMENTS. We thank Juliane Schelle and all other laboratory members for experimental help. We are grateful to I. Zerr and M. Schmitz (Goettingen, Germany), C. Glabe (Irvine, CA), Markus Fändrich (Ulm, Germany), and J. Morris and N. Cairns (St. Louis, MO) for help. This work was supported by grants from the EC Joint Programme on Neurodegenerative Diseases (JPND-REfrAME), the NIH (Grants P50-AG025688, RR00165, OD11132, and P30-AG010133), Public Health Service Grant P30-AG010133, the Alexander von Humboldt Foundation, the Göran Gustafsson Foundation, the Swedish Research Council, and the University College London Hospitals–National Institute for Health Research Biomedical Research Centre. T.L. is supported by a Senior Fellowship from Alzheimer's Research UK.

1. Morris JC (1999) Clinical presentation and course of Alzheimer disease. *Alzheimer Disease*, eds Terry RD, Katzman R, Bick KL, Sisodia SS (Lippincott Williams & Wilkins, Philadelphia), pp 11–24.
2. Nelson PT, et al. (2012) Correlation of Alzheimer disease neuropathologic changes with cognitive status: A review of the literature. *J Neuropathol Exp Neurol* 71: 362–381.
3. Lam B, Masellis M, Freedman M, Stuss DT, Black SE (2013) Clinical, imaging, and pathological heterogeneity of the Alzheimer's disease syndrome. *Alzheimers Res Ther* 5:1.
4. Ryan NS, et al. (2016) Clinical phenotype and genetic associations in autosomal dominant familial Alzheimer's disease: A case series. *Lancet Neurol* 15:1326–1335.
5. Hardy J, Selkoe DJ (2002) The amyloid hypothesis of Alzheimer's disease: Progress and problems on the road to therapeutics. *Science* 297:353–356.
6. Holtzman DM, Goate A, Kelly J, Sperling R (2011) Mapping the road forward in Alzheimer's disease. *Sci Transl Med* 3:114ps48.
7. Eisenberg D, Jucker M (2012) The amyloid state of proteins in human diseases. *Cell* 148:1188–1203.
8. Tycko R (2015) Amyloid polymorphism: Structural basis and neurobiological relevance. *Neuron* 86:632–645.
9. Meyer-Luehmann M, et al. (2006) Exogenous induction of cerebral beta-amyloidogenesis is governed by agent and host. *Science* 313:1781–1784.
10. Heilbronner G, et al. (2013) Seeded strain-like transmission of β-amyloid morphotypes in APP transgenic mice. *EMBO Rep* 14:1017–1022.
11. Watts JC, et al. (2014) Serial propagation of distinct strains of Aβ prions from Alzheimer's disease patients. *Proc Natl Acad Sci USA* 111:10323–10328.
12. Lu JX, et al. (2013) Molecular structure of β-amyloid fibrils in Alzheimer's disease brain tissue. *Cell* 154:1257–1268.
13. Qiang W, Yau WM, Lu JX, Collinge J, Tycko R (2017) Structural variation in amyloid-β fibrils from Alzheimer's disease clinical subtypes. *Nature* 541:217–221.
14. Cohen ML, et al. (2015) Rapidly progressive Alzheimer's disease features distinct structures of amyloid-β. *Brain* 138:1009–1022.
15. Rosen RF, et al. (2010) Deficient high-affinity binding of Pittsburgh compound B in a case of Alzheimer's disease. *Acta Neuropathol* 119:221–233.
16. Liu J, et al. (2016) Amyloid structure exhibits polymorphism on multiple length scales in human brain tissue. *Sci Rep* 6:33079.
17. Tagliavini F, Giaccone G, Frangione B, Bugiani O (1988) Preamyloid deposits in the cerebral cortex of patients with Alzheimer's disease and nondemented individuals. *Neurosci Lett* 93:191–196.
18. Yamaguchi H, Hirai S, Morimatsu M, Shoji M, Ihara Y (1988) A variety of cerebral amyloid deposits in the brains of the Alzheimer-type dementia demonstrated by beta protein immunostaining. *Acta Neuropathol* 76:541–549.
19. Ikeda S, Allsop D, Glenner GG (1989) Morphology and distribution of plaque and related deposits in the brains of Alzheimer's disease and control cases. An immunohistochemical study using amyloid beta-protein antibody. *Lab Invest* 60:113–122.
20. Wisniewski HM, Bancher C, Barcikowska M, Wen GY, Currie J (1989) Spectrum of morphological appearance of amyloid deposits in Alzheimer's disease. *Acta Neuropathol* 78:337–347.
21. Dickson TC, Vickers JC (2001) The morphological phenotype of beta-amyloid plaques and associated neuritic changes in Alzheimer's disease. *Neuroscience* 105:99–107.
22. Thal DR, Capetillo-Zarate E, Del Tredici K, Braak H (2006) The development of amyloid beta protein deposits in the aged brain. *Sci Aging Knowledge Environ* 2006:re1.
23. Maarouf CL, et al. (2008) Histopathological and molecular heterogeneity among individuals with dementia associated with Presenilin mutations. *Mol Neurodegener* 3: 20.
24. Walker LC (2016) Proteopathic strains and the heterogeneity of neurodegenerative diseases. *Annu Rev Genet* 50:329–346.
25. Aslund A, et al. (2009) Novel pentameric thiophene derivatives for in vitro and in vivo optical imaging of a plethora of protein aggregates in cerebral amyloidoses. *ACS Chem Biol* 4:673–684.
26. Wegenast-Braun BM, et al. (2012) Spectral discrimination of cerebral amyloid lesions after peripheral application of luminescent conjugated oligothiophenes. *Am J Pathol* 181:1953–1960.
27. Herrmann US, et al. (2015) Structure-based drug design identifies polythiophenes as antiprion compounds. *Sci Transl Med* 7:299ra123.
28. Bäck M, Appelqvist H, LeVine H, 3rd, Nilsson KP (2016) Anionic oligothiophenes compete for binding of X-34 but not PIB to recombinant Aβ amyloid fibrils and Alzheimer's disease brain-derived Aβ. *Chemistry* 22:18335–18338.
29. Psonka-Antonczyk KM, et al. (2016) Nanoscale structure and spectroscopic probing of Aβ1-40 fibril bundle formation. *Front Chem* 4:44.
30. Nyström S, et al. (2013) Evidence for age-dependent in vivo conformational rearrangement within Aβ amyloid deposits. *ACS Chem Biol* 8:1128–1133.
31. Langer F, et al. (2011) Soluble Aβ seeds are potent inducers of cerebral β-amyloid deposition. *J Neurosci* 31:14488–14495.
32. Stöhr J, et al. (2012) Purified and synthetic Alzheimer's amyloid beta (Aβ) prions. *Proc Natl Acad Sci USA* 109:11025–11030.
33. Ye L, et al. (2017) Aβ seeding potency peaks in the early stages of cerebral β-amyloidosis. *EMBO Rep* 18:1536–1544.
34. Schmidt M, et al. (2009) Comparison of Alzheimer Abeta(1-40) and Abeta(1-42) amyloid fibrils reveals similar protofilament structures. *Proc Natl Acad Sci USA* 106: 19813–19818.
35. Schmidt M, et al. (2015) Peptide dimer structure in an Aβ(1-42) fibril visualized with cryo-EM. *Proc Natl Acad Sci USA* 112:11858–11863.
36. Xiao Y, et al. (2015) Aβ(1-42) fibril structure illuminates self-recognition and replication of amyloid in Alzheimer's disease. *Nat Struct Mol Biol* 22:499–505.
37. Gremer L, et al. (2017) Fibril structure of amyloid-β(1-42) by cryo-electron microscopy. *Science* 358:116–119.
38. Condello C, Stohr J (March 28, 2017) Abeta propagation and strains: Implications for the phenotypic diversity in Alzheimer's disease. *Neurobiol Dis*, 10.1016/j.nbd.2017.03.014.
39. Näslund J, et al. (1994) Relative abundance of Alzheimer A beta amyloid peptide variants in Alzheimer disease and normal aging. *Proc Natl Acad Sci USA* 91: 8378–8382.
40. Portelius E, et al. (2010) Mass spectrometric characterization of brain amyloid beta isoform signatures in familial and sporadic Alzheimer's disease. *Acta Neuropathol* 120:185–193.
41. Crutch SJ, et al. (2017) Consensus classification of posterior cortical atrophy. *Alzheimers Dement* 13:870–884.
42. Magnusson K, et al. (2014) Multimodal fluorescence microscopy of prion strain specific PrP deposits stained by thiophene-based amyloid ligands. *Prion* 8:319–329.
43. Klingstedt T, et al. (2015) Distinct spacing between anionic groups: An essential chemical determinant for achieving thiophene-based ligands to distinguish β-amyloid or Tau polymorphic aggregates. *Chemistry* 21:9072–9082.
44. Jucker M, Walker LC (2013) Self-propagation of pathogenic protein aggregates in neurodegenerative diseases. *Nature* 501:45–51.
45. Li J, Browning S, Mahal SP, Oelschlegel AM, Weissmann C (2010) Darwinian evolution of prions in cell culture. *Science* 327:869–872.
46. Karran E, Mercken M, De Strooper B (2011) The amyloid cascade hypothesis for Alzheimer's disease: An appraisal for the development of therapeutics. *Nat Rev Drug Discov* 10:698–712.
47. Haass C, Selkoe DJ (2007) Soluble protein oligomers in neurodegeneration: Lessons from the Alzheimer's amyloid beta-peptide. *Nat Rev Mol Cell Biol* 8:101–112.
48. Portelius E, et al. (2007) Characterization of amyloid beta peptides in cerebrospinal fluid by an automated immunoprecipitation procedure followed by mass spectrometry. *J Proteome Res* 6:4433–4439.
49. Sturchler-Pierrat C, et al. (1997) Two amyloid precursor protein transgenic mouse models with Alzheimer disease-like pathology. *Proc Natl Acad Sci USA* 94: 13287–13292.
50. Eisele YS, et al. (2010) Peripherally applied Abeta-containing inoculates induce cerebral beta-amyloidosis. *Science* 330:980–982.
51. Bondolfi L, et al. (2002) Amyloid-associated neuron loss and gliogenesis in the neocortex of amyloid precursor protein transgenic mice. *J Neurosci* 22:515–522.

Supporting Information

Rasmussen et al. 10.1073/pnas.1713215114

SI Methods

Patient Samples. Tissue samples were obtained from the mid-temporal gyrus (temporal), pericalcarine gyri (occipital), and mid-frontal gyrus (frontal) of 40 clinically and pathologically diagnosed AD cases (Table S1). Among them, 13 familial cases (AD 1–13) had the following mutations: *V717I* in *APP*, three cases; *A431E* in *PSEN1*, three cases; *F105L* in *PSEN1*, two cases; and *E280A* in *PSEN1*, five cases. The remaining 27 cases had a typical sporadic (idiopathic) etiology (AD14–34) or a sporadic PCA variant of AD (AD35–40). The samples were obtained from four different sources, the Emory University Alzheimer's Disease Research Center; the Dementia Laboratory, Department of Pathology and Laboratory Medicine, Indiana University School of Medicine; the Queen Square Brain Bank at University College London; and the Institute of Medical Research, Faculty of Medicine, University of Antioquia, Medellín, Colombia. Human postmortem tissues were acquired under proper Institutional Review Board protocols with consent from families.

LCO Staining and Immunohistochemistry on Patient Samples. Two different LCO variants, qFTAA and hFTAA, were used for detection and analysis of amyloid pathology. Fresh-frozen human tissue was cut into 12-μm-thick sections on a cryotome, dried at room temperature (RT) overnight, and stored at −80 °C. Tissue was thawed, air-dried, and then double-stained with qFTAA and hFTAA (2.4 μM qFTAA and 0.77 μM hFTAA in PBS) similar to a previously described protocol (30). Sections were incubated for 30 min at RT in the dark.

Immunohistochemistry was performed using a polyclonal primary antibody directed against Aβ (CN6) as previously described (50). Staining with Congo red and Thioflavin-S for amyloid was conducted according to standard protocols.

Spectral Analysis. Spectra were acquired on a Zeiss LSM 510 META confocal microscope equipped with an argon 458-nm laser for excitation and a spectral detector (Carl Zeiss MicroImaging GmbH). A 40× oil-immersion objective (1.3 N.A.; Zeiss) was used for spectral imaging of Aβ-amyloid cores. Continuous emission spectra were acquired from 470 to 695 nm. The amyloid plaques were randomly chosen, and three regions of interest were measured in the core of each deposit (Figs. S1 and S2). Only the dense cores of plaques were analyzed. Other types of Aβ deposits (diffuse plaques, intracellular Aβ, and cerebral amyloid angiopathy) were excluded. Care was taken to avoid interference of lipofuscin-induced autofluorescence with LCO signals; the use of spectral imaging allowed us to distinguish between the distinct LCO fluorescence spectrum and unwanted autofluorescence.

A total of 15 to 25 Aβ plaque cores were measured in each region, totaling 45–60 plaques per patient. After the spectral measurements, all emission spectra were normalized to their respective maxima. The mean spectral signature of each plaque core was calculated before averaging the values for each brain area in each patient. The ratio of the intensity of emitted light at the blue-shifted peak (502 nm) and red-shifted peak (588 nm) was used as a parameter for spectral distinction of different Aβ deposits. The peaks of the spectra were selected to maximize the spectral distinction.

For the heat map of Euclidean distance calculation, the average spectrum from 470 nm to 695 nm was calculated for each brain region. Different spectra were then compared in two samples using the following Euclidean distance calculation:

$$\sqrt{\sum_{470nm}^{695nm}(ADx_{470nm}-ADy_{470nm})^2+\ldots+(ADx_{695nm}-ADy_{695nm})^2}.$$

In short, the "square-root of the sum-of-squared-differences" was calculated between two samples using the 22 wavelength measurements of fluorescence intensity. This pairwise calculation was completed for every sample pair used in the study. The output of these calculations is then displayed as a heat map, with larger and more darkly colored circles representing a large Euclidean distance (more different emission spectra). This heat map represents the comparison between samples for the entire emission curve. Further statistical comparisons between samples were undertaken using the ratio of the fluorescence intensity at two wavelengths (502 nm/588 nm) representing the peaks of fluorescence for the two dyes used in this study. The Euclidean distance calculation and the heat map were generated in R (v. 3.3.2).

ECL-Based Multiarray for Aβ Quantification. Human tissue was homogenized in PBS (10% wt/vol) using the Precellys system with a 2 × 20-s cycle at 5,500 rpm (Precellys24 Homogenizer, EQ03119-200-RD000.0, Bertin Instruments). Samples were then extracted with 70% formic acid (final concentration) and centrifuged at 25,000 × *g* for 60 min at 4 °C. Supernatants were collected and neutralized with buffer (1 M Tris base, 0.5 M Na_2NPO_4, 0.05% NaN_3) before analysis with a V-PLEX Peptide Panel 1 (6E10) Aβ kit from Meso Scale Discovery following the manufacturer's specifications.

PK Digestion. Samples homogenized with the Precellys system described previously were centrifuged at 800 × *g* for 5 min at 4 °C, and the supernatant was collected. Protein concentrations were determined using a bicinchoninic acid total protein kit, and samples were then digested with 1 μg of PK/3 μg of protein at 37 °C. Samples were collected for analysis at 0, 1, 2, and 4 h and stopped with 2 mM PMSF. Samples were heated to 70 °C for 10 min in LDS sample buffer (Invitrogen), loaded onto 4–12% Bis-Tris precast gels, and run at 125 V for 44 min. Gels were transferred onto nitrocellulose and subsequently boiled at 95 °C for 5 min in PBS. Blocking was achieved with 4% skim milk in PBS with 0.05% Tween-20 for 60 min at RT. Membranes were probed with antibody 6E10 (1:5,000) overnight at 4 °C and then incubated with a goat anti-mouse secondary antibody (1:30,000) for 60 min. Development was carried out with Dura Extended Duration Substrate (Pierce) before exposure on Hyperfilm ECL film (Amersham). Band intensities were quantified using ImageJ software (NIH).

Mass Spectrometry. Human tissue was homogenized in PBS (10% wt/vol) using the Precellys system with a 2 × 20-s cycle at 5,500 rpm (Precellys24 Homogenizer, EQ03119-200-RD000.0, Bertin Instruments). Samples were then extracted with 70% formic acid, centrifuged at 25,000 × *g* for 60 min at 4 °C, and dried in a speedvac. The samples were reconstituted in 200 μL of formic acid for 30 min and then neutralized to pH 7 using 0.5 M Tris. Aβs were then immunoprecipitated using Aβ-specific antibodies [antibodies 6E10 and 4G8 (Signet Laboratories)] coupled to magnetic Dynabeads M-280 Sheep Anti-Mouse IgG (Invitrogen) as described previously (48). Mass spectrometry was performed using a MALDI TOF/TOF instrument (UltraFleXtreme; Bruker Daltonics). Analysis was completed as described previously (48).

In Vivo Inoculations. Given that the LCO spectral characteristics of plaque cores did not differ among the three brain regions, we prepared the donor inoculum from temporal cortical samples only. Seeding extracts were generated from a 10% (wt/vol) homogenate of the middle temporal gyrus using the Precellys system as described above. The homogenates were subsequently centrifuged at 3,000 × *g* for 5 min at 4 °C. The supernatants were then collected and stored at −80 °C. Quantification of Aβ in the extracts was performed after formic acid extraction using the MesoScale platform. Seeding extracts were pooled for the *APP V717I* (AD1–3), *PSEN1 A431E* (AD4–6), and typical sAD (AD15, AD16, and AD24) groups (Table S1), while the PiB-refractory case remained distinct. All samples then were adjusted to the same total Aβ concentration (7.5 pg/mL) using PBS as a diluent.

Predepositing 4-mo-old female APP23 mice (49) were injected bilaterally (2.5 μL each) with seeding extracts from the *APP V717I* ($n = 6$), *PSEN1 A431E* ($n = 7$), typical sAD ($n = 8$), and PiB-negative sAD ($n = 6$) cases following anesthesia with ketamine/xylazine (100 mg/kg to 10 mg/kg of body weight). Injections were targeted to the hippocampus (anteroposterior, −2.5 mm; left/right, ±2.0 mm; dorsoventral, −1.8 mm) and delivered with a Hamilton syringe at a speed of 1.25 μL/min. The syringe was kept in place for an additional 2 min and then slowly withdrawn. The surgical incision then was closed, and the mice were closely monitored until regaining consciousness. All experimental procedures with the mice were carried out in accordance with the veterinary office regulations of Baden-Württemberg (Germany) and approved by the local animal care and use committees (Regierungspräsidium Tübingen).

Histological Analysis of the Mice. After 6 mo of incubation following infusion of brain extracts, the mice were killed by deep anesthesia (250 mg/kg ketamine and 25 mg/kg xylazine) and transcardial perfusion with ice-cold PBS. The brains were immersion-fixed in 4% paraformaldehyde-PBS for 48 h and then cryoprotected in 30% sucrose-PBS. After snap-freezing in methyl butane, brains were sectioned at 25-μm thickness on a freezing-sliding microtome (Microm; Thermo Scientific) and collected in 12-well plates (every 12th section was represented in a well) containing cryoprotectant solution (35% ethylene glycerol and 25% glycerol in PBS). Sections were immunostained for Aβ using either a polyclonal antibody (discussed above) and Vectastain Elite ABC kit (Vector Laboratories) (50) or the double-stain LCO protocol outlined for the human tissue (discussed above).

The hippocampus (every 12th section) of each animal was analyzed for the area occupied by Aβ-positive immunostaining with stereological analysis on a video-microscopy system (Zeiss Axioskop 2) equipped with a motorized *x-y-z* stage and Stereo Investigator software (MicroBrightField) as previously described (51). The area occupied by Aβ-positive staining was determined using 2D sectors in a single focal plane (magnification of 20×/0.45-N.A. objective) as sampling sites.

Statistical Analysis. To test normality, the D'Agostino–Pearson omnibus normality test was used. For two-way ANOVA followed by Tukey's multiple comparisons test, data were logarithmically transformed when not normally distributed. The nonparametric Spearman correlation or Kruskal–Wallis test followed by Dunn's multiple comparison test were used in all other analyses. GraphPad Prism (v.5) was used for all statistical analyses.

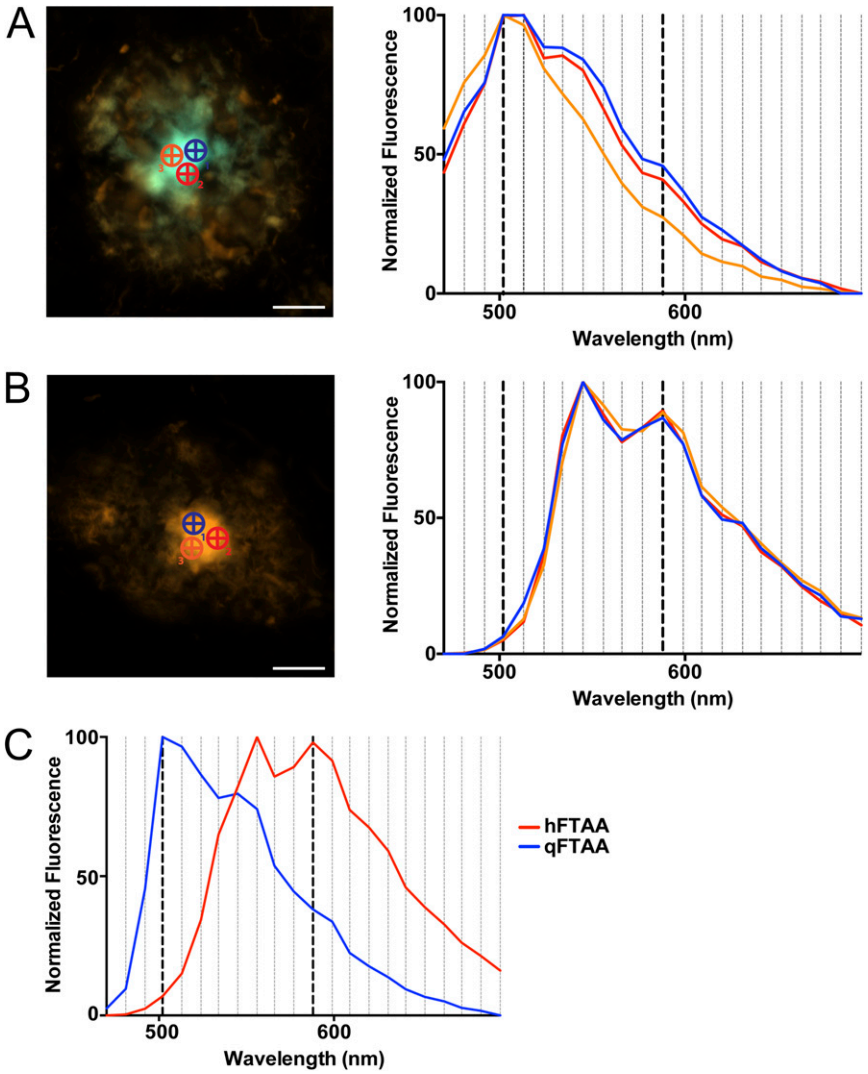

Fig. S1. Analysis of LCO-stained amyloid plaque cores. (*A* and *B*) Two representative images of the temporal cortical region of a sAD case (AD16) that was stained with hFTAA and qFTAA. For each plaque core, three regions of interest (circle/cross symbols) were set and the fluorescence intensity was measured at 22 wavelengths. A plaque core with an emission peak in the blue spectrum is shown in *A*, whereas *B* shows a plaque core with an emission peak in the red spectrum. For each plaque core, the mean was calculated from the three regions of interest. Diffuse plaques, cerebral amyloid angiopathy, and intracellular aggregates were not included in this analysis. (Scale bars: 20 μm.) (*C*) For comparative illustration, the spectra of the single-LCO dyes hFTAA and qFTAA are shown. Single staining with either hFTAA or qFTAA was performed on three different patients (AD17, AD20, and AD23), and the individual spectra were calculated from 60 different plaques. qFTAA shows a peak around 500 nm, whereas hFTAA shows two peaks around 550 and 590 nm.

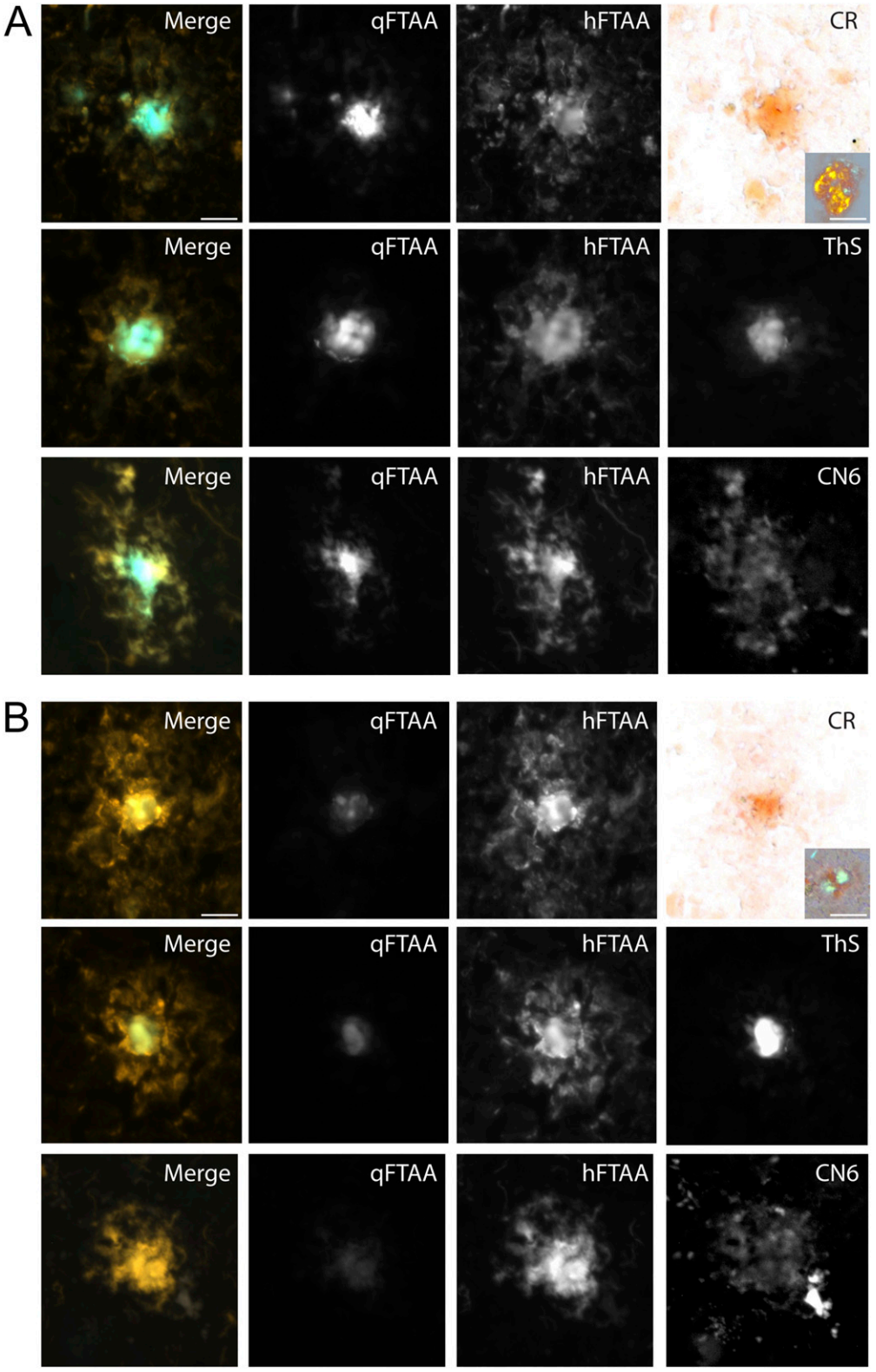

Fig. S2. Double staining of LCOs combined with other amyloid markers. Tissue from a sAD case (AD17) was stained with hFTAA and qFTAA and in adjacent sections with Congo Red (CR), Thioflavin-S (ThS), or the polyclonal Aβ antibody CN6. (*A*) Three blue-shifted plaques are shown with adjacent sections stained for CR (*Inset* shows birefringence), ThS, or CN6. (*B*) Three red-shifted plaques are shown with adjacent sections stained for CR (*Inset* shows birefringence), ThS, or CN6. No differences in staining between the blue- and red-shifted plaque (cores) were detected with CR, ThS, or the Aβ antibody. (Scale bars: 20 μm.)

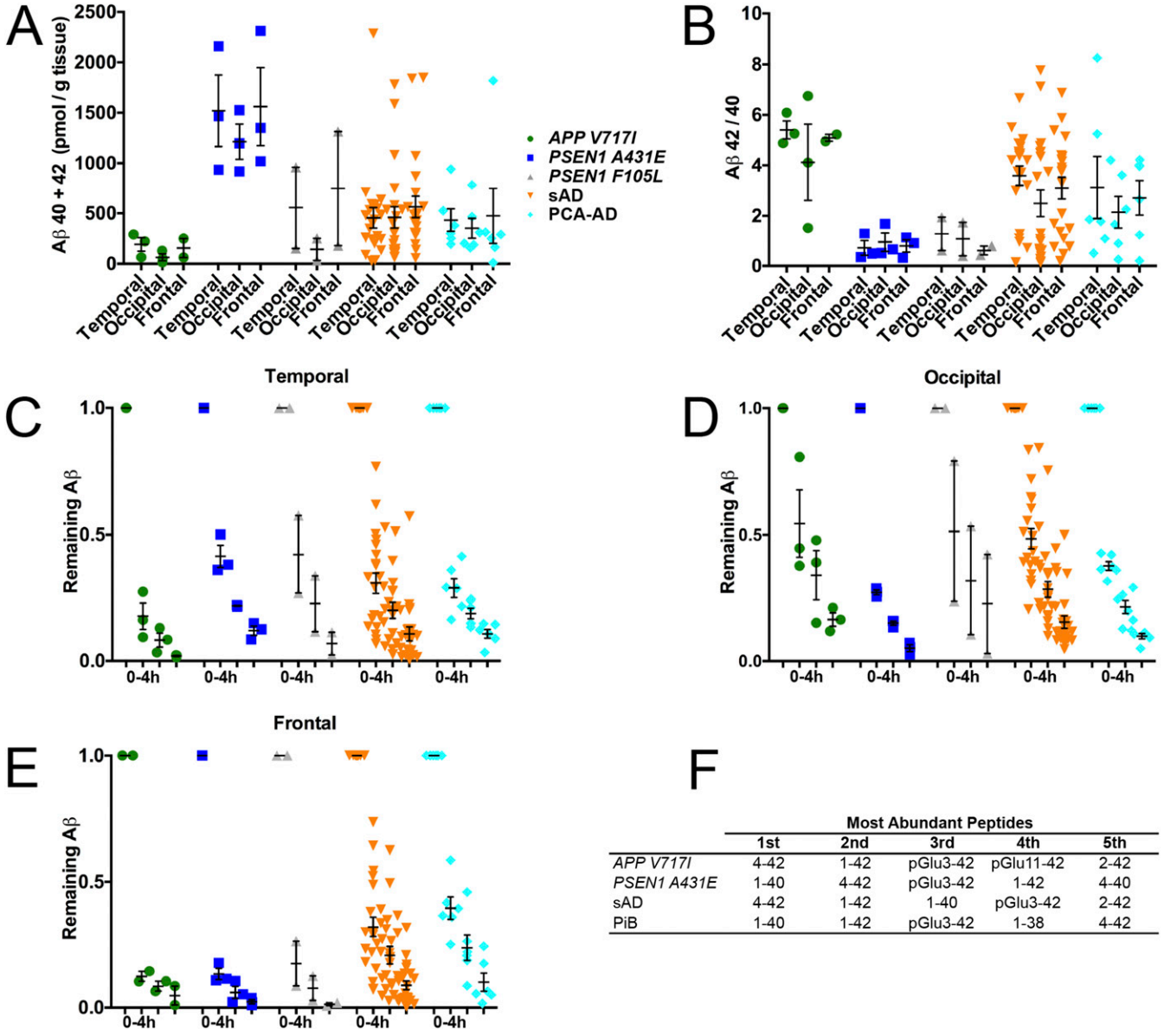

	Most Abundant Peptides				
	1st	2nd	3rd	4th	5th
APP V717I	4-42	1-42	pGlu3-42	pGlu11-42	2-42
PSEN1 A431E	1-40	4-42	pGlu3-42	1-42	4-40
sAD	4-42	1-42	1-40	pGlu3-42	2-42
PiB	1-40	1-42	pGlu3-42	1-38	4-42

Fig. S3. Biochemical analysis of brain tissue from different AD subtypes. Levels of total Aβ40 + Aβ42 (*A*) and Aβ 42/40 ratio (*B*) for each patient (formic acid extraction before 25,000 × *g* centrifugation) were assessed by ECL-based multiarray. Two-way ANOVA (brain region × subtype) revealed significantly different levels of Aβ among AD subtypes [$F_{(4,89)} = 8.278$, $P < 0.0001$], but no significant differences among brain regions [$F_{(2,89)} = 2.375$, $P = 0.0989$]. No subtype × region interaction was found [$F_{(8,89)} = 0.8558$, $P = 0.5568$]. Tukey's multiple comparisons test revealed significant differences in total Aβ between *APP V717I* vs. *PSEN1 A431E* and sAD; *PSEN1 A431E* vs. *PSEN1 F105L*, sAD, and PCA-AD (all probabilities at least $P < 0.05$). Two-way ANOVA also revealed significantly different Aβ42/40 ratios in the AD subtypes [$F_{(4,89)} = 4.744$, $P = 0.0016$], but no significant differences among brain regions [$F_{(2,89)} = 0.3785$, $P = 0.6860$] or in the subtype × region interaction [$F_{(8,89)} = 0.2835$, $P = 0.9698$]. Tukey's multiple comparisons test revealed significant differences in the Aβ42/40 ratio between *APP V717I* vs. *PSEN1 A431E* and *PSEN1 F105L*; *PSEN1 A431E* vs. sAD (all probabilities at least $P < 0.05$). (*C*–*E*) PK digestion of brain samples was used to determine protease resistance of Aβ over time (0, 1, 2, and 4 h), expressed as the fraction remaining after digestion compared with the undigested sample. Brain regions were analyzed individually. No significant differences were found among patient subtypes using two-way ANOVA (time × subtype) for the temporal [$F_{(4,30)} = 1.197$, $P = 0.3325$], occipital [$F_{(4,30)} = 2.080$, $P = 0.1083$], or frontal [$F_{(4,29)} = 2.184$, $P = 0.0957$] region. Significant differences for the time effect were seen in the temporal [$F_{(3,90)} = 106.7$, $P < 0.0001$], occipital [$F_{(3,90)} = 152.9$, $P < 0.0001$], and frontal [$F_{(3,87)} = 134.5$, $P < 0.0001$] regions. Interactions were not significant in the temporal [$F_{(12,90)} = 1.351$, $P = 0.2049$], occipital [$F_{(12,90)} = 1.211$, $P = 0.2877$], or frontal [$F_{(12,87)} = 1.717$, $P = 0.0767$] region. Note that *PSEN1 E280A* cases were not included for biochemical analysis because fresh-frozen tissue samples were not available when other measurements were completed. (*F*) Mass spectrometry analysis of the brain samples used for injections (Fig. 3) revealed that all samples contained Aβ1–42, Aβ4–42, and pGlu3–42, with *APP V717I* samples containing additional Aβx–42 peptide species and patients with *PSEN1 A431E* and sAD harboring Aβ1–40. The PiB refractory case also had abundant Aβ1–40 as well as Aβ1–38 in the tissue.

Table S1. Patient information

Case	Etiology	Age, y	Sex	PMI, h	ApoE status
AD1	*APP V717I*	45	M	4.0	n.a.
AD2	*APP V717I*	49	F	2.7	E3/3
AD3	*APP V717I*	54	F	5.3	E3/3
AD4	*PSEN1 A431E*	43	F	4.0	E3/3
AD5	*PSEN1 A431E*	47	n.a.	n.a.	E3/3
AD6	*PSEN1 A431E*	44	M	n.a.	E3/3
AD7	*PSEN1 F105L*	68	F	36.0	E2/3
AD8	*PSEN1 F105L*	67	F	8.0	E2/3
AD9	*PSEN1 E280A*	52	M	4.8	E3/3
AD10	*PSEN1 E280A*	42	F	6.5	E3/3
AD11	*PSEN1 E280A*	63	F	6.5	E3/3
AD12	*PSEN1 E280A*	63	M	3.8	E3/3
AD13	*PSEN1 E280A*	58	M	3.5	E3/3
AD14	sAD	80	F	25.8	n.a.
AD15	sAD	62	M	8.5	E2/3
AD16	sAD	81	F	17.7	E3/3
AD17	sAD	70	M	8.5	E3/3
AD18	sAD	81	F	n.a.	E3/3
AD19	sAD	62	F	6.0	E3/3
AD20	sAD	74	M	2.5	E3/3
AD21	sAD	54	M	5.5	E3/3
AD22	sAD	91	F	3.0	E3/3
AD23	sAD	81	M	4.0	E3/3
AD24	sAD	89	M	49.0	E3/4
AD25	sAD	64	M	9.0	E3/4
AD26	sAD	87	F	6.0	E3/4
AD27	sAD	58	F	6.0	E3/4
AD28	sAD	77	M	6.0	E3/4
AD29	sAD	88	M	9.0	E3/4
AD30	sAD	70	F	46.9	E3/3
AD31	sAD	67	M	28.6	n.a.
AD32	sAD	77	M	90.1	E4/4
AD33	sAD	76	F	26.8	n.a.
AD34*	sAD	72	F	3.0	E3/4
AD35	PCA-AD	76	M	50.3	E3/3
AD36	PCA-AD	71	M	57.5	E3/4
AD37	PCA-AD	68	F	86.8	E3/4
AD38	PCA-AD	88	F	40.3	E3/3
AD39	PCA-AD	71	M	47.6	E3/3
AD40	PCA-AD	65	F	46.6	n.a.

F, female; M, male; n.a., information not available.
*PiB-negative sAD case: AD34.